A comparative experimental and multiphysics computational fluid dynamics study of coupled surface–subsurface flow in bed forms

Felix Janssen,[1] M. Bayani Cardenas,[2] Audrey H. Sawyer,[2,3] Thea Dammrich,[1,4] Jana Krietsch,[1,5] and Dirk de Beer[1]

Received 14 February 2012; revised 11 June 2012; accepted 21 June 2012; published 21 August 2012.

[1] The use of multiphysics computational fluid dynamics (CFD) approaches to simulate surface–subsurface flow processes is evaluated by comparison with flume experiments on current-exposed permeable bed forms. The unique experimental data include measurements of the time-averaged surface water flow velocities, the pressure distribution at the sediment–water interface, and pore water flow paths. The modeling approach first simulates the time-averaged turbulent flow in the channel with CFD and then uses the predicted pressure distribution at the sediment–water interface to drive a flow and transport model for the sediment. The CFD-modeled velocity and pressure distribution and transient particle tracks within the sediment agree reasonably well with observations. Differences that exist between observations and simulations mainly concern the eddies in the wake zone downstream of the ripple crests that are slightly shorter than those predicted by the model. This deviation propagates from the surface to the subsurface domain, appearing in the pressure distribution along the bed and, consequently, the subsurface flow patterns. The good representation of general patterns and rates makes multiphysics CFD modeling a powerful and sufficiently accurate tool that can replace measurements for many studies of surface–subsurface processes involving current-exposed immobile bed forms. The approach can be used for predicting transport processes where they cannot easily be observed, such as in large rivers and coastal systems where boundary conditions such as mean currents and bed forms can be mapped.

Citation: Janssen, F., M. B. Cardenas, A. H. Sawyer, T. Dammrich, J. Krietsch, and D. de Beer (2012), A comparative experimental and multiphysics computational fluid dynamics study of coupled surface–subsurface flow in bed forms, *Water Resour. Res.*, *48*, W08514, doi:10.1029/2012WR011982.

1. Introduction

[2] Detailed measurements of hydrologic processes are difficult to obtain under natural conditions due to methodological limitations. An example of such a process is the local-scale transport of fluids and solutes across coupled surface and subsurface systems, such as rivers and their underlying and adjacent sediment (the hyporheic zone) or permeable sediments that are exposed to tidal and wind-driven bottom flow in coastal marine systems. In order to study such complicated processes, hydrologists have historically turned to computational and experimental models. In the case of the coupled surface–subsurface exchange, the models must consider the multiphysics nature of the studied process where several coupled partial differential equations are needed for the proper description of the conservation of momentum and mass.

[3] Flow through permeable sediments is driven by pressure gradients along the sediment–water interface. Pressure gradients may be due to differences in hydrostatic pressure (as typically assumed in large-scale modeling of river–aquifer interactions), or nonhydrostatic contributions, which are driven at the local scale by the redirection of fluid momentum associated with turbulent flow over a nonflat bed. The process is referred to as "pumping" or "current-induced advective transport" in the literature on fluvial or marine systems, respectively. It is now widely accepted as one of the main drivers for subsurface flow through bed forms, from ripple to pool-riffle scales [*Elliott and Brooks*, 1997a; *Huettel and Webster*, 2001].

[4] The concept of coupled surface–subsurface flows was first proposed in the context of fish spawning by *Vaux* [1968] as part of his investigations of interstitial flow through gravel beds. He recognized the connection between hydrodynamic conditions in the stream and the pressure distribution at the sediment–water interface: Because of continuity of pressure across the stream–gravel interface, the potential at the upper bed boundary must be equal to the potential at the bottom of the contiguous flowing stream. The problem of determining the potential along the upper

[1]Max Planck Institute for Marine Microbiology, Bremen, Germany.
[2]Geological Sciences, University of Texas at Austin, Austin, Texas, USA.
[3]Now at Geological Sciences, University of Delaware, Newark, Delaware, USA.
[4]Now at Alfred Wegener Institute for Polar and Marine Research, Wadden Sea Station Sylt, List, Germany.
[5]Now at Laval University Cancer Research Center, Quebec City, Quebec, Canada.

Corresponding author: F. Janssen, Max Planck Institute for Marine Microbiology, Celsiusstr. 1, D-28359 Bremen, Germany. (fjanssen@mpi-bremen.de)

0043-1397/12/2012WR011982

boundary then becomes one of hydraulics. Based on the analytical solution of the groundwater flow equation and Darcy's Law, and on electrical analogue experiments, Vaux suggested that upwelling and downwelling patterns would occur due to local head variations. Almost two decades later, *Thibodeaux and Boyle* [1987] provided first experimental evidence. They conducted dye tracer experiments in a 55 cm long gravel bed form with a 5 cm high crest that was subject to open channel flow of ~50 cm/s. Their results illustrated downwelling of water at the stoss side of the bed form (i.e., the upstream face in front of the crest) with upwelling at the lee side (the downstream face behind the crest) and flow convergence toward the crest. They attributed the convergence of flow toward the crest to a pressure drop associated with a vortex in the lee side of the bed form. This study was followed by complementary numerical modeling studies [*Savant et al.*, 1987] that imposed observed pressure distributions along the stoss surface of triangular forms taken from previous resistance studies [*Vittal et al.*, 1977] as boundary conditions.

[5] Measurements by *Fehlman* [1985] and *Shen et al.* [1990] refined our understanding of the distribution of nonhydrostatic pressure along the surface of a triangular form subject to unidirectional water flow. Pressure gradually increases along the stoss face of the bed form, peaks around the middle of the stoss face, drops toward a pressure minimum at the crest, and remains low along the lee face and the trough until the pressure begins to increase again at the stoss face of the following ripple. A key result of the study was a scaling equation which relates channel velocity, water column height, and bed form geometry to the amplitude of the pressure change across the bed form. Based on Fehlman's results, *Elliott and Brooks* [1997a, 1997b] developed an analytical model for subsurface flow that is largely similar to the Tóth solution for regional groundwater flow [*Toth*, 1963; *Zlotnik et al.*, 2011]. Elliott and Brooks' model imposes a sinusoidal pressure boundary with an amplitude calculated according to Fehlman's scaling equation along a flat sediment surface. This model has been the basis for several recent studies of hydrodynamics and chemistry of porous river beds [*Boano et al.*, 2007, 2010; *Marion et al.*, 2008; *Packman et al.*, 2000; *Ren and Packman*, 2005; *Salehin et al.*, 2004] and has been recently extended or modified for three-dimensional exchange [*Stonedahl et al.*, 2010; *Tonina and Buffington*, 2007; *Worman et al.*, 2006].

[6] While pioneering flume experiments focused on the mechanics of subsurface flow, more recent flume experiments have investigated transport and transformation of metals, nutrients, and particulate organic matter [*Franke et al.*, 2006; *Huettel et al.*, 1998; *Packman and MacKay*, 2003; *Precht et al.*, 2004]. Other flume-based studies have considered more realistic heterogeneous properties of streambed sediment [*Marion et al.*, 2008; *Salehin et al.*, 2004] and more complex obstacles or topographic features driving surface–subsurface exchange [*Endreny et al.*, 2011; *Mutz et al.*, 2007; *Sawyer et al.*, 2011]. Advances in observational technology continue to lead toward better and more detailed understanding of subsurface transport processes in both space and time [*Chen et al.*, 2008, 2009; *Precht et al.*, 2004; *Reidenbach et al.*, 2010].

[7] In recent years, the focus of research on surface–subsurface systems has been on processes within the bed with little to no emphasis on hydraulics of the open channel. However, as *Vaux* [1968] suggested, determining the pressure distribution which drives pumping is really a "hydraulics problem." Coupled or linked physics-based modeling approaches that represent flow and transport in the open channel and sediment with sufficient accuracy have been used to address this problem and further quantify coupled surface and subsurface processes [*Cardenas and Wilson*, 2007b; *Cardenas et al.*, 2008a]. Extensions of this approach have included analysis of the effects of small-scale variation in sediment permeability [*Sawyer and Cardenas*, 2009], channel covers [*Cardenas and Gooseff*, 2008], salmon redds [*Tonina and Buffington*, 2009], and obstructions such as logs [*Sawyer et al.*, 2011]. Other models have addressed heat transport [*Cardenas and Wilson*, 2007a, 2007b; *Sawyer et al.*, 2012], filtration of fine particles [*Karwan and Saiers*, 2012], multispecies reactive transport [*Bardini et al.*, 2012; *Cardenas et al.*, 2008b], variable density flow [*Jin et al.*, 2011], and turbulent, transient conditions where sediment elastic properties become important [*Cardenas and Jiang*, 2011]. Others have used single-domain models of turbulent flow and porous media flow (represented by increased drag where porous media are present) to analyze hyporheic exchange underneath in-stream structures forming steps [*Endreny et al.*, 2011; *Crispell and Endreny*, 2009].

[8] Modeling-based studies by *Cardenas and Wilson* [2007b] reproduced some of the experiments of *Elliott and Brooks* [1997b] and data on turbulent velocity fields over dunes reasonably well. Moreover, the selected simulation approach was able to replicate the pressure distribution measured by *Fehlman* [1985]. Using a similar approach, *Sawyer et al.* [2011] demonstrated agreement between measured and simulated pressure distributions and subsurface flow paths associated with open-channel flow around a channel obstruction. With increasing computing power and ever more sophisticated algorithms, computational fluid dynamics (CFD) simulations are expected to become more useful and accessible tools for analysis of coupled surface and subsurface processes. However, a systematic appraisal of multiphysics CFD approaches based on a robust comparison to a fully comprehensive experimental data set of a coupled surface–subsurface system is still missing.

[9] This study uses a combination of modeling and experiments to test the application of multiphysics CFD modeling for investigations of coupled surface–subsurface processes and to address the question if simulations may render tedious and resource-intensive laboratory experiments unnecessary. Flume experiments are conducted in which key parameters are either precisely controlled or comprehensively measured using minimally invasive methods. The entire experimental section of the flume is simulated numerically with the measured parameters as boundary or domain conditions. This allows for a one-to-one comparison and a systematic analysis of the performance of multiphysics CFD modeling across the two domains.

2. Methods

2.1. Flume Experiment Setup

[10] Experiments were conducted in a 2 m long and 0.3 m wide recirculating glass flume with a 1.5 m long test section (Figure 1). The bottom of the channel was filled with well-sorted silicate construction sand (Busch Quarz, Schnaittenbach,

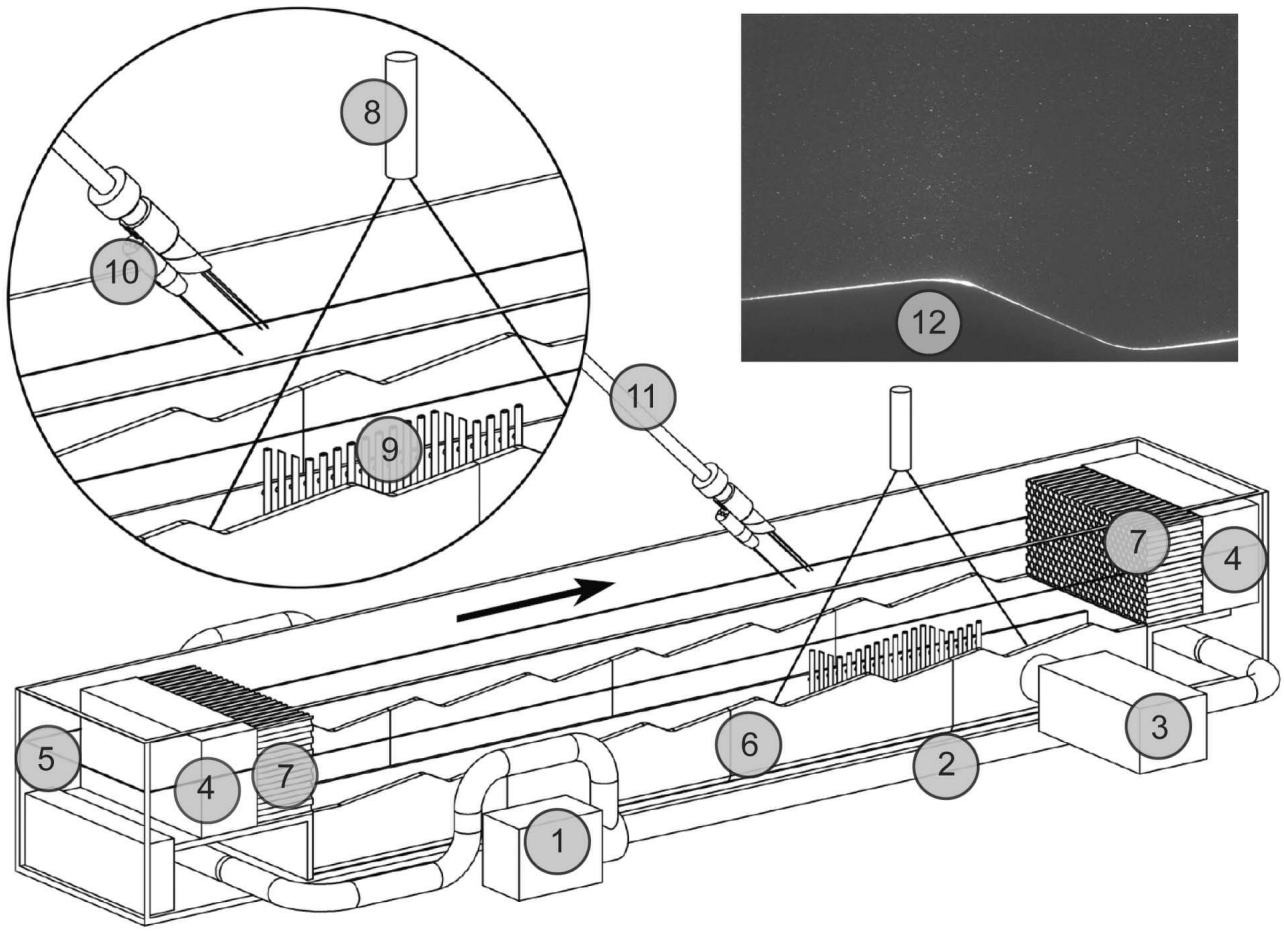

Figure 1. Experimental setup. The numbers correspond to (1) pump, (2) water recirculation line, (3) fast shutter camera used for particle image velocimetry (PIV), (4) polyester filter foam, (5) water surface, (6) ripple stencil, (7) polycarbonate honeycomb flow rectifier, (8) line laser for projecting vertical laser sheet for PIV, (9) pressure ports on support plate, (10) sensor head with injection needle and two fiber-optic fluorescence sensors, (11) rod controlled by precision gears, and (12) sample PIV image of neutrally buoyant particles taken by (3) and illuminated by (8).

Germany) with a mean grain size of 0.174 mm, a standard deviation of 0.15 mm, a porosity of 0.4, and a permeability of 1.5×10^{-11} m^2 as determined by constant head permeametry. Seven identical current-type ripples (height = 2 cm, length = 20 cm, trough to crest distance = 15 cm) with rounded troughs and crests (radius of curvature = 2 cm) were shaped into the sand bed (Figures 1, 2a, and 2c). The rippled surface was fringed on the upstream and downstream end by 5 cm long planar sections. Low-frequency vibrations of ~4 Hz were applied to the flume by means of a ballast-laden shaker table fixed to the flume stand while filling in the sand to compact the bed reproducibly. To facilitate ripple shaping, 1 cm wide CAD-milled PVC ripple stencils were positioned along the sidewalls of the test section, reducing the width of the sand bed to 28 cm (Figures 1 and 2). Sand depth beneath troughs was 9 cm. Measurements of open channel flow velocity, pressure distributions at the bed surface, and pore water flow patterns within the bed focused on the sixth ripple, i.e., the second-to-last ripple toward the downstream end of the test section (the "test ripple"). Water depth (z) was 10 cm above troughs. Water was recirculated by one and two centrifugal pumps in one or two recirculation lines, respectively (Figure 1). This resulted in a "low-discharge" (2.1 L s^{-1}) and a "high-discharge" (3.6 L s^{-1}) setting with corresponding mean horizontal flow velocities (U_{ave}) of 7 cm s^{-1} and 12 cm s^{-1}, respectively. Taking the ripple height as characteristic length scale, these settings were equivalent to Reynolds numbers of ~1300 and ~2400, respectively. To stabilize and rectify the flow, 10 and 5 cm thick blocks of 10 pores per inch polyester filter foam (E. Hennecken GmbH, Stolberg, Germany) and polycarbonate honeycomb (cell diameter 4.5×10^{-3} m, Plascore, Waldlaubersheim, Germany) were installed upstream and downstream of the test section of the flume, respectively (Figure 1). The open channel flow was subcritical with the sand remaining immobile at both flow settings. The water temperature was 17°C, corresponding to density of 998.8 kg m^{-3}, and kinematic viscosity was 1.1×10^{-6} m^2 s^{-1}.

2.1.1. Particle Image Velocimetry of Open Channel Flow

[11] The open channel flow velocity distributions along the length and height of the water column (u, w) were characterized by particle image velocimetry (PIV). Measurements were performed along the midline of the flume in the region of the test ripple at both discharge settings (Figure 1). Additional measurements were performed in the

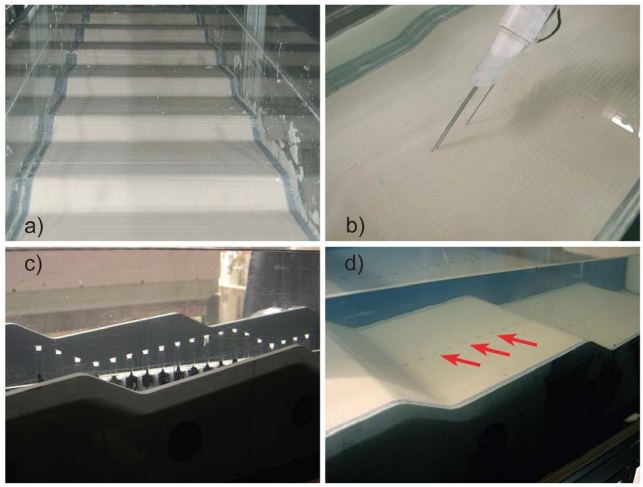

Figure 2. Pictures of the experimental setup. (a) Bed surface, shaped with the ripple stencil visible at both sidewalls of the flume. (b) Sensor head during injection of the fluorescent dye within the sand. (c) Pressure measurement setup prior to filling the working section with sand and (d) after filling in and shaping the sand. The pressure ports (red arrows point at three of them) are flush with the bed surface.

region of the leading planar section directly downstream of the honeycomb flow straightener. Approximately neutrally buoyant white Polyamide particles (~30 μm particle size, Vestosint 1164, Evonik Industries, Essen, Germany) were added to the water. A diode laser (Lasiris SNF 660 nm, 35 mW with line optics, StockerYale Canada Inc., Montreal, CA) was positioned above the water surface and projected a <1 mm wide laser sheet along the x-z plane in the midline of the flume (Figure 1). The laser sheet was in the focus of a monochrome electrically cooled fast shutter 1280 × 1024 pixel CCD camera (SensiCam, PCO Computer Optics, Kehlheim, Germany) attached to the side of the flume (sample image in Figure 1 inset). A custom-built controlling unit synchronized the camera shutter to the laser and triggered two laser pulses resulting in pairs of images of the moving particles. The camera field of view of 12 cm × 9 cm (width × height) extended from the sediment surface to slightly below the water surface at a resolution of ~10 pixel mm^{-1}. For both flow settings, seven series of images were recorded at camera positions spaced by 5 cm along the length of the flume, resulting in an overlap of ~60% in images from neighboring camera positions. The total field of view of the combined images spanned ~40 cm including the entire test ripple as well as the lee and stoss sides of the fifth and seventh ripple, respectively. Forty replicate image pairs (4 ms exposure time) were taken at each camera position at 10 and 6 ms laser pulse spacing for the slow and fast flow setting, respectively. Image analysis was done on the respective image pairs by means of a PIV analysis software (VidPIV, Intelligent Laser Applications, Juelich, Germany) with a correlation window size of 32 × 32 pixels and a correlation window spacing of 16 pixels. Velocities were calculated from horizontal and vertical correlation window shift divided by image resolution and laser pulse spacing. Outliers in the velocities were detected based on predefined ranges in velocity (u: −35 to 180% of U, w: −35 to 35% of W, where u and w denote instantaneous velocities in x and y directions and the capital U and W time-averaged velocities) and correlation signal-to-noise ratio (SNR) determined by the VidPIV software. Thresholds for velocity and correlation SNR were adjusted manually based on a visual assessment of vector plots of the instantaneous velocity distributions until all obvious outliers were identified. After removing the outliers, median velocity components u_{med} and w_{med} were calculated for each correlation window location. Median velocities from each camera position were pooled and interpolated on a 5 × 2 mm grid along the length and height of the water column, respectively.

2.1.2. Pressure Measurements

[12] The pressure distribution at the sediment-water interface was determined experimentally at both the slow and fast flow setting. A total of 19 pressure ports were installed at a spacing of 16.33 mm along the midline of the test ripple between the crest of the fifth ripple and the stoss face of the seventh ripple (Figures 1 and 2c). Each port consisted of a vertical glass tube (7 mm outer diameter, 1 mm wall thickness). The port openings at the upper end of the glass tubes were covered by a 3 mm thick insert of sintered glass frit material. The wall of the glass tube and the sintered glass insert were ground flush with the slope of the sand surface at the respective positions of the rippled bed (Figures 2c and 2d). The glass tubes were attached to a vertical PVC support plate that was installed in the sand bed along the midline of the flume. Within the sand bed 8 mm × 5 mm (OD × ID) PVC tubing was attached to the lower end of each glass tube, connecting the individual pressure ports to a multiport manifold outside of the flume. The tubes left the sand bed and the flume in upward direction directly downstream of the inlet, i.e., far away from the test section. To minimize interference with the flow the 19 tubes were combined to two flat bundles of 10 and 9 tubes, respectively that were glued to the inner surface of the respective sidewalls (not shown in Figure 1). Over a short distance (~80 mm) the two 8 mm thick tube bundles reduced the total channel width by 16 mm (<6%). By means of individual valves installed close to the manifold the pressure ports were successively connected to a wet/wet differential pressure transducer to determine the pressures relative to a stagnant water reservoir aside of the flume. The entire setup (glass tubes, PVC tubing, PVC plate) was only installed in experimental runs dedicated to pressure measurements and removed from the sand bed for measurements of open channel flow and pore water flow.

2.1.3. Pore Water Flow and Transport Tracing

[13] Pore water flow patterns and velocities were determined with a dye tracer displacement technique. Fluorescent dye was injected at predefined points within the bed and the location of the clouds of stained pore water was mapped in the end of the respective experimental runs by multiple fluorescence profiling with fiber optical sensors (Figures 1 and 2b). Unlike previous flume experiments [e.g., *Elliott and Brooks*, 1997b; *Packman and MacKay*, 2003; *Ren and Packman*, 2005; *Sawyer et al.*, 2011; *Endreny et al.*, 2011], this allowed for measurements along the channel midline, which eliminates effects due to the flume walls.

[14] The core apparatus consisted of an array of a 1.1 mm diameter dye injection needle with two 0.5 μm wide lateral openings close to the cone-shaped tip and two 120 mm long fluorescence sensors with 0.6 mm wide tips (number 10 in Figure 1). Multimode glass fibers (100/140 μM diameter) that were glued into stainless steel tubing and polished flush

with the surface at the tip served as fluorescence sensors. To improve fluorescence sensor stiffness, the 0.6 mm steel tubing was glued into stainless steel tubing sections of increasing thickness up to an outer diameter of 2 mm at the sensor holder. Both excitation light and fluorescence traveled through the same fiber. The optical setup was similar to that of *Precht and Huettel* [2004] and consisted of a blue light-emitting diode with a 450–490 nm filter for excitation, a wavelength division fiber coupler, and a photomultiplier tube with a 515–560 nm filter to sense the fluorescence intensity. Injection needle and fluorescence sensors were attached to the end of a rod that could be translated precisely at an angle of 45° relative to the water surface by means of a single axis linear drive. This "sensor lance" was attached to an automated horizontal carriage rail on top of the flume to allow for accurate positioning along the midline of the flume.

[15] Approximately 300 μL of a 50 mg L^{-1} sodium fluorescein (Uranine) solution were injected into the sediment at predefined positions by means of a peristaltic pump connected to the injection needle. The dye injection/profiling array was retracted from the water column to minimize disturbance of the flow while the experiment was running. After turning off the flow, diagonal fluorescence profiling with the lance drive was repeated at consecutive horizontal positions. This resulted in a grid of fluorescence measurements with a spacing of 2.5 and 0.6 mm in x and z direction, respectively. The sediment in the test section was removed and washed after each run and the ripples were reshaped.

[16] A total of 16 experimental runs were performed, 6 at slow and 10 at fast flow settings. Injections took place at discrete points in the bed below the test ripple at 2 and 4 cm below the sediment-water interface (see enumeration in Figure 8 (top)). For the low-discharge experiments, dye was injected at 14 locations and the flow ran for 10 and 12 h, respectively. At high-discharge conditions, injections took place at 10 positions and the flow ran for 1, 2, 3, 4, and 6 h in the different experimental runs. The center of the dye cloud was determined as the center of mass of the distribution of fluorescence (i.e., dye concentration) along the midline of the flume. The shift in dye cloud position between the locations of injection and detection was determined relative to reference measurements performed in experiments without flow to account for any dislocation of the stained pore water by the fluorescence sensors during profiling. Dye cloud displacement was not corrected for retardation of the fluorescent dye by adsorption to sediment particles or other reactions (e.g., complexation, precipitation). As no obvious tails were recognized in the dye clouds that were mapped after being transported with the pore waters it is assumed that the dye did not interact substantially with the sediment used in this study. Nevertheless, some retardation of sodium fluorescein in aquifers was reported from lab and field transport studies [*Vereecken et al.*, 1999; *Mojid and Vereecken*, 2005]. Therefore, the dye cloud displacement has to be considered a conservative estimate of the true pore water displacement.

2.2. Numerical Modeling Methods

[17] The computational modeling approach follows that of *Cardenas and Wilson* [2007b] where the model for the surface water flow and pore water flow are sequentially coupled. The turbulent flow model is run separately, and the results for pressure along the sediment-water interface are used as boundary conditions for the pore water flow model.

2.2.1. Computational Fluid Dynamics Simulations of Turbulent Flow

[18] Turbulent flow in the test section of the flume was simulated by numerically solving a finite-volume formulation of the Reynolds-averaged Navier-Stokes (RANS) equations for an incompressible, homogeneous fluid:

$$\frac{\partial U_i}{\partial x_i} = 0 \tag{1}$$

$$\rho U_j \frac{\partial U_i}{\partial x_j} = -\frac{\partial P}{\partial x_i} + \frac{\partial}{\partial x_j}\left(2\mu S_{ij} - \rho\overline{u_j' u_i'}\right) \tag{2}$$

where ρ and μ are fluid density and dynamic viscosity, t is time, $U_{i\,or\,j}$ (i, j = 1, 2 where $i \neq j$) is the time-averaged velocity, u_i' (i = 1, 2) are the fluctuations in the instantaneous velocity components in $x_{i\,or\,j}$ (i, j = 1, 2 where $i \neq j$) directions, and P is time-averaged pressure. S_{ij} is the strain rate tensor defined as:

$$S_{ij} = \frac{1}{2}\left(\frac{\partial U_i}{\partial x_j} + \frac{\partial U_j}{\partial x_i}\right). \tag{3}$$

The Reynolds stresses are related to the mean strain rates by:

$$\tau_{ij} = -\overline{u_j' u_i'} = \nu_t(2S_{ij}) - \frac{2}{3}\delta_{ij}k \tag{4}$$

where ν_t (or μ_t/ρ) is the kinematic eddy viscosity, δ_{ij} is the Kronecker delta, and k is turbulent kinetic energy. The RANS equations were coupled to the k-ω turbulence closure scheme [*Wilcox*, 1998] since it has been demonstrated to accurately capture recirculation zones at the lee side of ripples. The eddy viscosity in this closure scheme is:

$$\nu_t = \frac{k}{\omega} \tag{5}$$

where the specific dissipation, ω, is the ratio of the turbulence dissipation rate ε to k:

$$\omega = \frac{\varepsilon}{\beta^* k} \tag{6}$$

and β^* is a closure coefficient. The steady state transport equations for k and ω are:

$$\rho\frac{\partial(U_j k)}{\partial x_j} = \rho\tau_{ij}\frac{\partial U_i}{\partial x_j} - \beta^*\rho\omega k + \frac{\partial}{\partial x_j}\left[(\mu + \mu_t\sigma_k)\frac{\partial k}{\partial x_j}\right], \tag{7}$$

$$\rho\frac{\partial(U_j \omega)}{\partial x_j} = \alpha\frac{\rho\omega}{k}\tau_{ij}\frac{\partial U_i}{\partial x_j} - \beta\rho\omega^2 + \frac{\partial}{\partial x_j}\left[(\mu + \mu_t\sigma_\omega)\frac{\partial \omega}{\partial x_j}\right]. \tag{8}$$

β^* is given by:

$$\beta^* = \beta_0^* f_{\beta^*}, \text{ where} \tag{9}$$

$$f_{\beta^*} = \frac{1 + 680\chi_k^2}{1 + 400\chi_k^2} \text{ for } \chi_k > 0 \text{ and } 1 \text{ for } \chi_k \leq 0. \tag{10}$$

Table 1. List of Simulation Cases With Different Boundary Conditions

Case	Inlet Boundary Condition	Wall Boundary Condition	Wall Boundary
1	mass flux	smooth/no roughness	fine
2	prescribed velocity	smooth/no roughness	fine
3	prescribed velocity	smooth/no roughness	coarse (node y = 2 mm)
4	prescribed velocity	roughness height = 0.35 mm	fine
5	prescribed velocity	roughness height = 0.35 mm	coarse (node y = 2 mm)

χ_k is defined as:

$$\chi_k = \frac{1}{\omega^3}\frac{\partial k}{\partial x_j}\frac{\partial \omega}{\partial x_j}. \quad (11)$$

Closure coefficients are standard values: α = 13/25, β = 9/125, β_0^* = 9/100, and $\sigma_k = \sigma_\omega = 0.5$.

[19] A symmetry boundary was used at the top of the water column, effectively making this an "enclosed flow" problem (the free surface is treated as a slip or shear-free wall, which is appropriate for open-channel flows with planar free surface). The water depth in the channel is large enough to replace the free surface in the simulation with the symmetry condition (water column Froude numbers, using the water column depth as the characteristic length, are $\ll$1 in all simulations). Since the flume used here has a short test section and planar bed sections near the inlet and outlet, the inlets and outlets could not be paired as periodic boundary conditions, unlike in previous generalized modeling studies [e.g., *Cardenas and Wilson*, 2007b]. Models with different boundary conditions for the inlet/outlet were compared including mass flux inlet/outflow outlet (referred to as Case 1), and specified inlet velocity profiles/specified pressure outlets (Cases 2–5). Unlike Cases 2–5, the inlet velocity profile in Case 1 is uniform, and outlet pressure and velocity evolve according to interior flow conditions. The lower boundary (i.e., the sediment-water interface) is treated as a wall boundary in all simulations. To investigate the significance of different wall conditions for the CFD results, both smooth (Cases 2–3) and rough walls (Cases 4–5) were compared. Additionally, the effect of different wall-adjacent cell heights was investigated. Cases 2 and 4 use a fine near-wall mesh that resolves the viscous sublayer (cell height <1 mm). Cases 3 and 5 use a coarse near-wall mesh with a node size of 2 mm at the boundary (i.e., several times the sediment grain diameter). This effectively places the cell centroid above the grain tops in Case 5. In rough wall simulations (Cases 4 and 5), the roughness height is 0.35 mm, or about twice the median grain diameter in flume experiments. The five cases that were analyzed are described in Table 1. The finite-volume simulation was conducted with the CFD software FLUENT (ANSYS Inc., Canonsburg, PA, USA; see www.ansys.com).

2.2.2. Pore Water Flow Simulations and Particle Tracing

[20] Two-dimensional pore water flow in the sand was modeled by solving the steady state groundwater flow equation:

$$\nabla \cdot \left(-\frac{k}{\mu} \nabla \cdot P \right) = 0 \quad (12)$$

where k is isotropic permeability, μ is viscosity, and P is pressure; the parenthetical term is the Darcy flux or Darcy velocity (Q). The solution from turbulent flow simulations for pressure along the sediment-water interface is prescribed as a Dirichlet boundary at the top of the porous domain. All other boundaries in the porous flow simulation correspond to flume walls and are prescribed as no flow boundaries. After division by porosity the resultant flow field was used as input for particle tracking which ignores dispersion since the study primarily focuses on the advective flow paths. The pore water flow simulation was conducted with the finite element code COMSOL Multiphysics (COMSOL, Inc., Burlington, MA, USA; see www.comsol.com).

3. Results

3.1. Experimental and Simulated Channel Velocity Fields

[21] The open circles in Figures 3 and 4 show measured profiles of horizontal flow velocities at different positions in the region of the test ripple (sixth ripple; see Figure 1) for the low- and high-discharge case, respectively. Detachment of the flow starts immediately downstream of the crest (Figures 3c, 3m, 4c, and 4m), i.e., at the point where the layer of reduced flow velocities in the vicinity of the sediment surface starts to broaden. Further downstream, an eddy with recirculating flow develops and reaches its maximum vertical size at the position of the trough (Figures 3e, 3o, 4e, and 4o). Downstream from the trough, the eddy diminishes until the flow reattaches at positions g and q at the lower stoss face of the ripples, where the steep velocity gradient at the sediment surface reestablishes. Apart from the different mean velocities, the main difference between the two discharge cases is the slightly larger vertical extension of the eddy in the low-discharge case. The decrease in measured velocity toward the water surface, visible in the low-discharge case, is an artifact due to air bubbles being trapped and blocking some of the upper cells of the honeycomb flow rectifier.

[22] RANS simulations of turbulent flow in the flume describe the measured mean velocity fields reasonably well for both low- and high-discharge settings. The eddy at the lee side of the ripple is readily captured by the simulated channel flow. Especially in the low-discharge case, however, the simulations overestimate the eddy length and height and predict reattachment of the flow further downstream than the measurements (Figures 3f–3h, 3n–3r, 4f–4h, and 4n–4r).

[23] For both discharge cases the velocity field is generally simulated more accurately for Cases 2–5 (colored lines in Figures 3 and 4) when the RANS model is prescribed a quadratic inlet velocity profile. The quadratic function was adjusted to the overall volumetric flow at the low- and high-discharge cases, and measured velocity profiles near the inlet matched the quadratic profiles reasonably well. Employing general mass flux boundary conditions for the inlet in simulation Cases 1 (black dashed line in Figures 3 and 4) resulted in stronger deviations that affected the entire profiles, especially for the high-discharge conditions. Simulation Cases 2 and 3 indicate some effect of the wall-adjacent cell height. Case 3 (coarse wall-adjacent mesh) shows a smaller eddy (see Figures 4e–4h) as compared to Case 2 where meshes at the boundary were smaller. The velocity fields in Cases 2 and 3 become more similar with distance

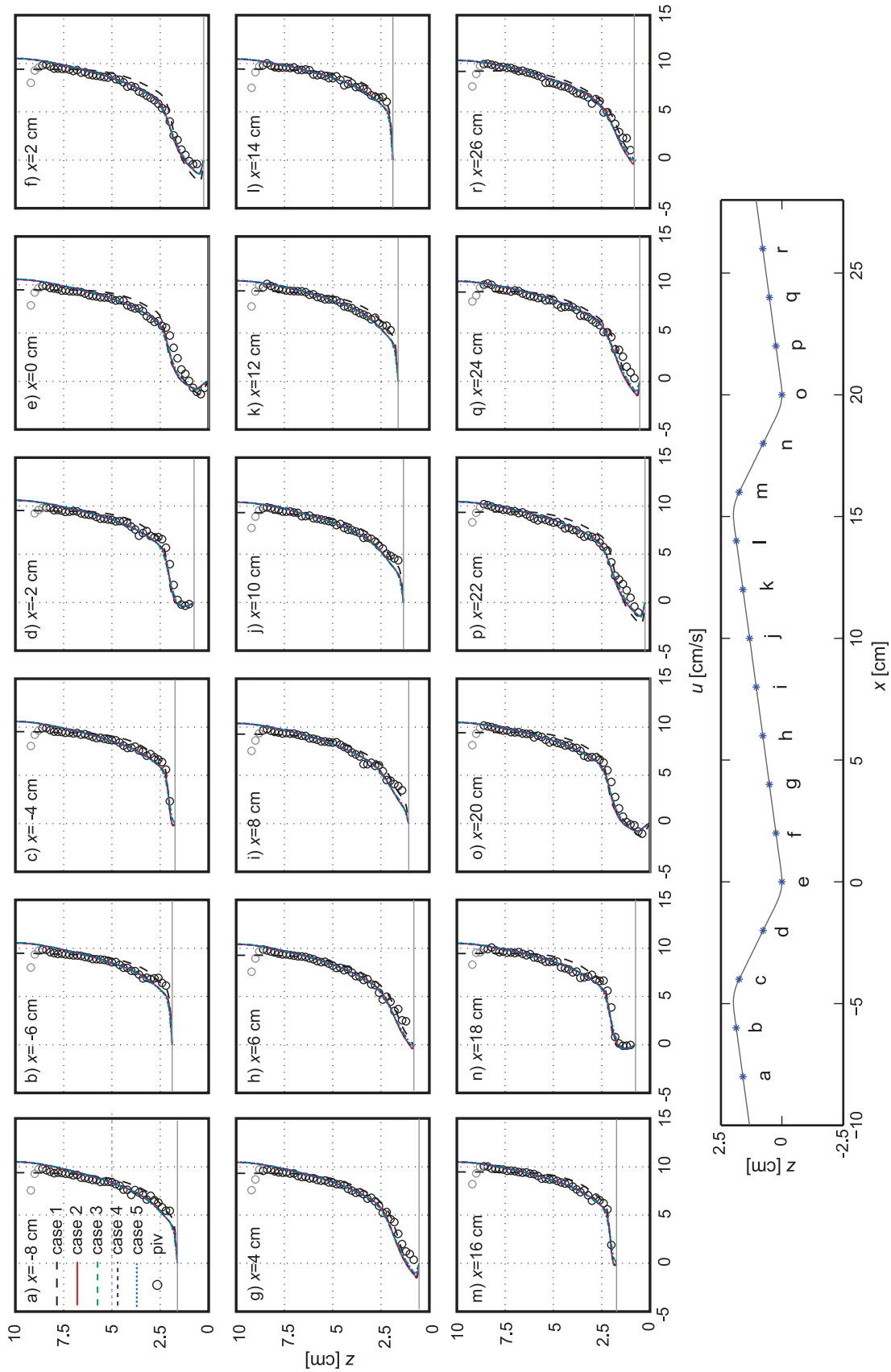

Figure 3. Comparison of measured and modeled velocity profiles over the test ripple for the "low-discharge" case. The modeled velocities are for the five cases described in Table 1. The vertical gray line denotes the location of the sediment-water interface. (bottom) The locations of the profiles are denoted by the blue asterisk labeled with the corresponding subplot letters.

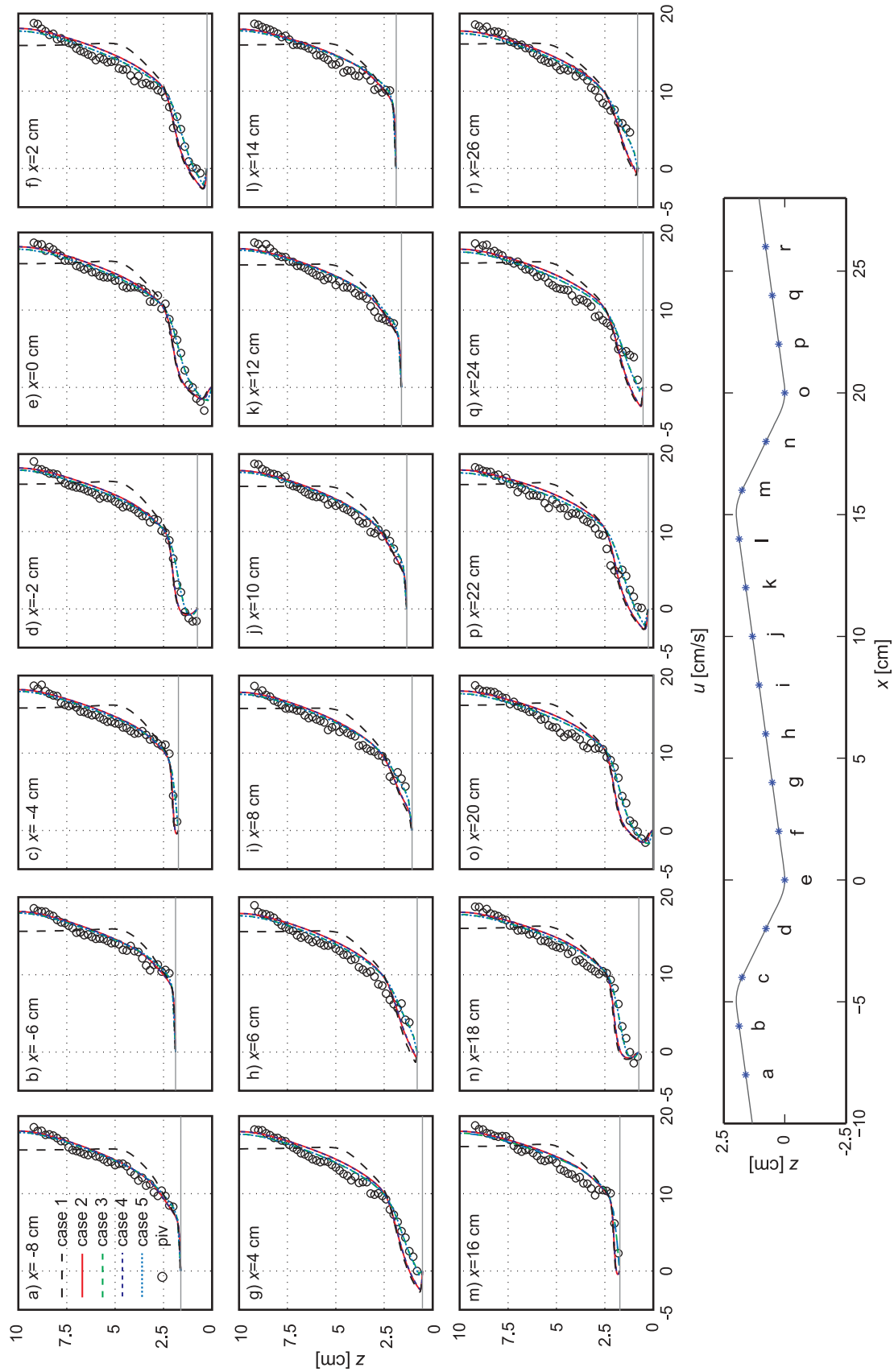

Figure 4. Comparison of measured and modeled velocity profiles over the test ripple for the "high-discharge" case. The modeled velocities are for the five cases described in Table 1. The vertical gray line denotes location of the sediment-water interface. (bottom) The locations of the profiles are denoted by the blue asterisk labeled with the corresponding subplot letters.

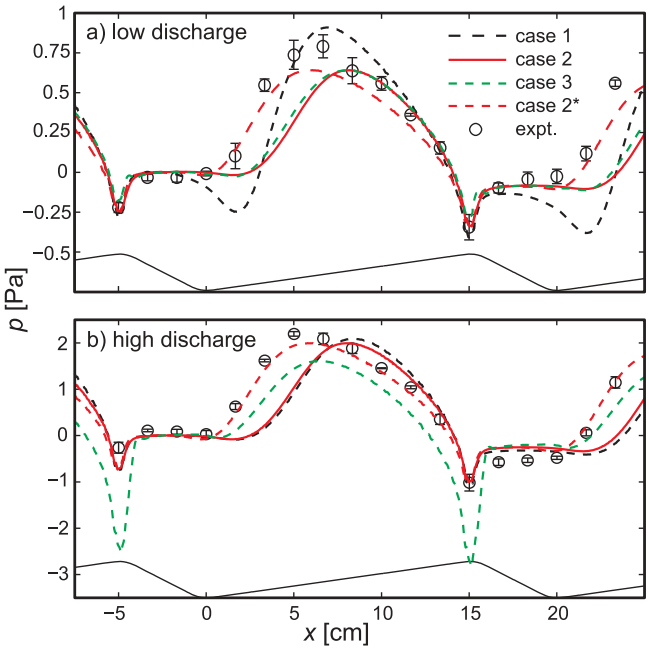

Figure 5. Comparison of modeled and measured pressure along the sediment–water interface of the test ripple for (a) low-discharge and (b) high-discharge scenarios for Cases 1, 2 (two runs each), and 3. The second version of Case 2, denoted 2*, has a pressure profile shifted locally (see section 3.4). The circles denote the average of three replicate pressure measurements, and the error bars denote the standard deviation. Pressures are given relative to the pressure at $x = -2.5$ cm at the lee side of the fifth ripple to facilitate comparisons.

from the wall, i.e., in the bulk flow. Moreover, the differences between Cases 2 and 3 are less pronounced in the low-discharge scenario. The effect of wall roughness on the simulated velocity fields is negligible, as profiles simulated with the same grids but different wall roughness are indistinguishable. This is true for the smooth and rough wall simulations ran with fine mesh (Cases 2 and 4) as well as for those adopting the coarse mesh (Cases 3 and 5).

3.2. Experimental and Simulated Interfacial Pressures

[24] Replicate measurements of interfacial pressures along the wall boundary (i.e., the sediment-water interface) in the region of the test ripple (open circles in Figures 5a and 5b) showed only small deviations. This is, to our knowledge, the first set of pressure measurements obtained along unconsolidated permeable sandy bed forms with a realistic geometry with rounded crests and troughs. As expected, the amplitude of the pressure peak is larger at higher discharge, while the overall patterns of the pressure distributions are similar for both flow settings. A sharp pressure minimum in the region of the crest where the flow detaches to form an eddy ($x = -5$ cm) is followed by a plateau that spans the lee face of the bed form and the region of the trough. At the lower part of the stoss face the pressure starts to increase and forms a broad pressure peak with a maximum at the position where the flow reattaches ($x \sim 5$ cm). Further downstream, the pressure decreases and finally gives way to the following pressure dip at the next crest.

[25] The form of the simulated pressure profiles is qualitatively similar for all simulations (Figure 6) and in good agreement with the measurements in the region of the test ripple (Figure 5). Most of the simulations predict the size of the pressure dip fairly well while they generally underestimate

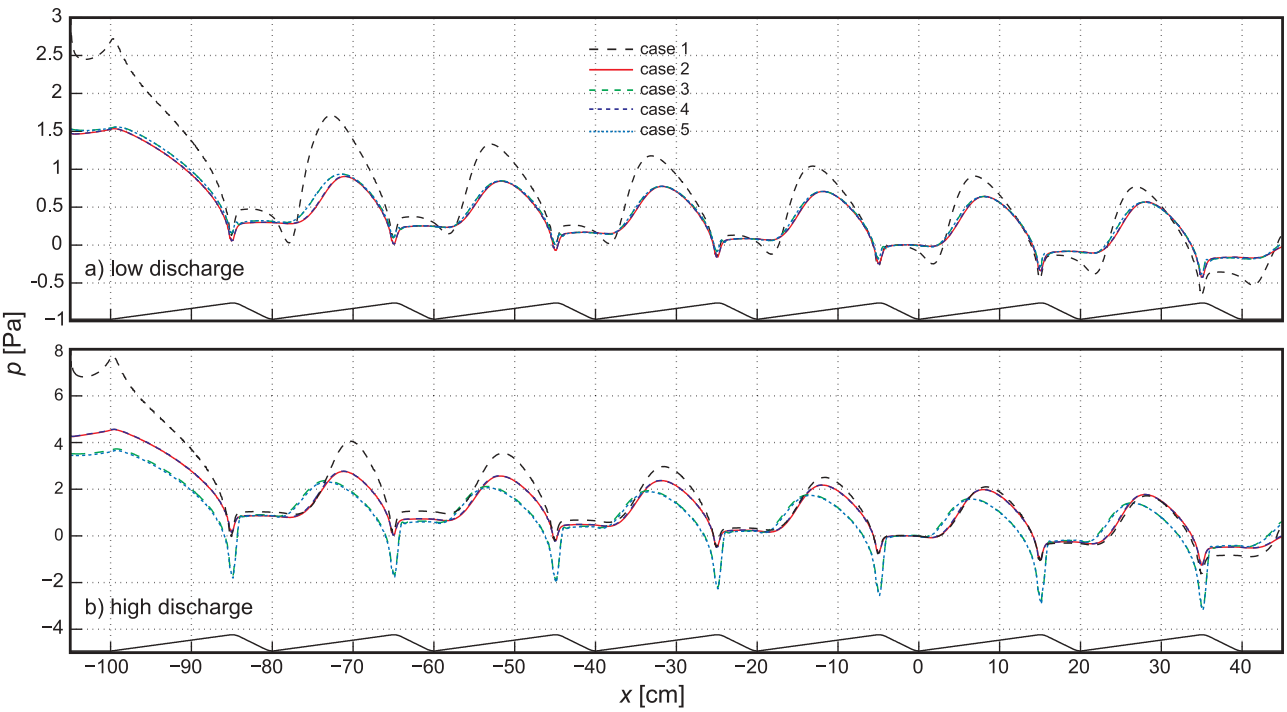

Figure 6. Modeled pressure distribution along the sediment-water interface for (a) low-discharge and (b) high-discharge scenarios for the five different boundary condition cases shown in Table 1 (and in Figures 3 and 4). The sediment topography is included in the plots. Pressures are given relative to the pressure at $x = -2.5$ cm at the lee side of the fifth ripple to facilitate comparisons.

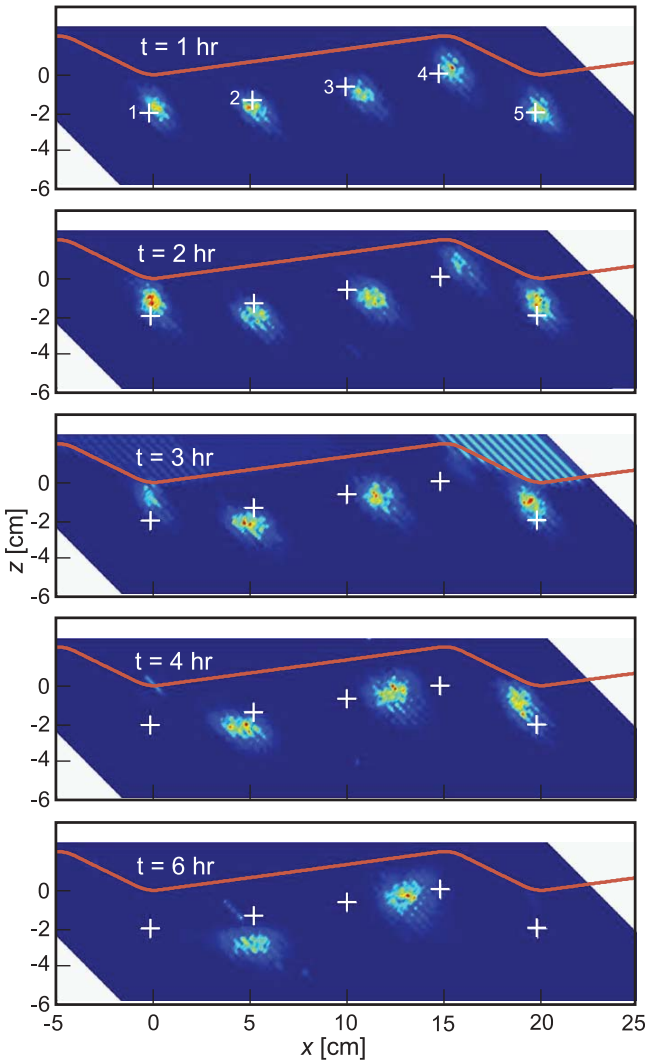

Figure 7. False-color plots of measured dye tracer concentration in the sediment after different periods of flow (t, run time of pumps) for the high-discharge experiment. Each panel represents a separate experimental run. White crosses indicate injection points (x, z at t = 0 h). Note that some dye plumes had already left the sediment after longer periods of flow (injection points 1, 4, and 5).

the magnitude of the pressure peak, especially at low discharge. The effect of wall roughness on simulated pressure profiles was negligible (fine mesh Cases 2 and 4 and coarse mesh Cases 3 and 5 in Figure 6). For this reason, the following description only discriminates between results of the fine mesh and the coarse mesh simulations, represented by Case 2 and 3 in Figure 5, respectively. Case 2* represents a modified case that is discussed in section 3.4.

[26] The best agreement between modeled and measured pressure distributions exists for the simulations with prescribed inlet velocities under low-discharge conditions (Figure 5a). Here the simulated pressures are within the standard deviation of the pressure measurements for more than half of the measured locations. Low-discharge simulations were insensitive to mesh size. For high-discharge conditions, there is a clear effect of the mesh size with a more pronounced pressure dip in the simulation with coarse mesh (Case 3) that clearly disagrees with measurements (Figure 5b). Simulations with a fine mesh (Case 2) match the measurements fairly well.

[27] Generally, the deviations of the simulated pressure distributions from measurements correspond to differences that exist between simulated and measured velocity fields (section 3.1). The onset of the pressure rise and the location of the pressure peak are clearly shifted downstream for most of the simulated pressures. This relates directly to the overestimation of the eddy size and to the reattachment of the flow further downstream in simulations. In Case 3 simulations at high-discharge flow reattachment occurred further upstream than in the other cases (Figures 4g and 4h) which agrees better with the experiments. In this case better agreement is also found in terms of pressure peak location (Figure 5b). Simulations with general mass flux boundary conditions for the inlet (Case 1) consistently poorly represented velocity and pressure distributions especially at low discharge. Here the simulated pressure peaks exceed measurements and all other simulated peaks (Figures 5a and 6a). Furthermore, the profile exhibits a strong secondary pressure dip right before the pressure rise (e.g., at $x \sim 1.7$ cm) that is absent in the measured distributions and the other simulations. At high discharge (Figures 5b and 6b) the secondary pressure dip is absent for Case 1, and the pronounced pressure peaks only exist in the upstream part of the test section but decay toward the downstream end of the bed. At the sixth ripple, the Case 1 pressure profiles are largely similar to those simulated with the fine mesh (Figure 5b, Case 2) and agree fairly well to measurements.

3.3. Experimental and Simulated Pore Water Flow Fields

[28] The displacement of injected fluorescein dye was mapped effectively by the dye displacement technique (Figure 7). The plumes spread almost symmetrically, facilitating the detection of the center of mass of the dye plumes.

[29] For both the low- and high-discharge case the dye displacement indicates qualitatively similar flow fields. This is evident when measured dye tracks (connected open circles in Figure 8) are superimposed with the simulated pore water flow fields (curved blue lines in Figure 8). The dye tracks signify a pore water flow field that clearly separates into two counter-rotating flow cells which divide in the lower half of the stoss face. In this region, where the flow reattaches and pressure maxima are found, the dye tracks indicate a strong downward component of the pore water flow. Upstream of this location, pore water flows clockwise toward the upstream crest while counter-clockwise circulation toward the downstream crest is found downstream of the flow cell divide. As expected from the pressure profiles, pore water velocities increased with channel velocity: The farthest distances traveled by the dye plumes at the respective locations are generally larger under high (Figures 8e–8h) than low discharge (Figures 8a–8d) despite the fact that dye tracks at high discharge only represent half the time (6 h of flow instead of 12 h).

[30] Differences in pore water velocities between low and high discharge are also captured by the simulations and encompass the entire test section (Figure 9). The different inlet boundary and wall conditions used in the turbulent flow models, which led to differences in the pressure profiles (Figure 6), only result in relatively small differences in the

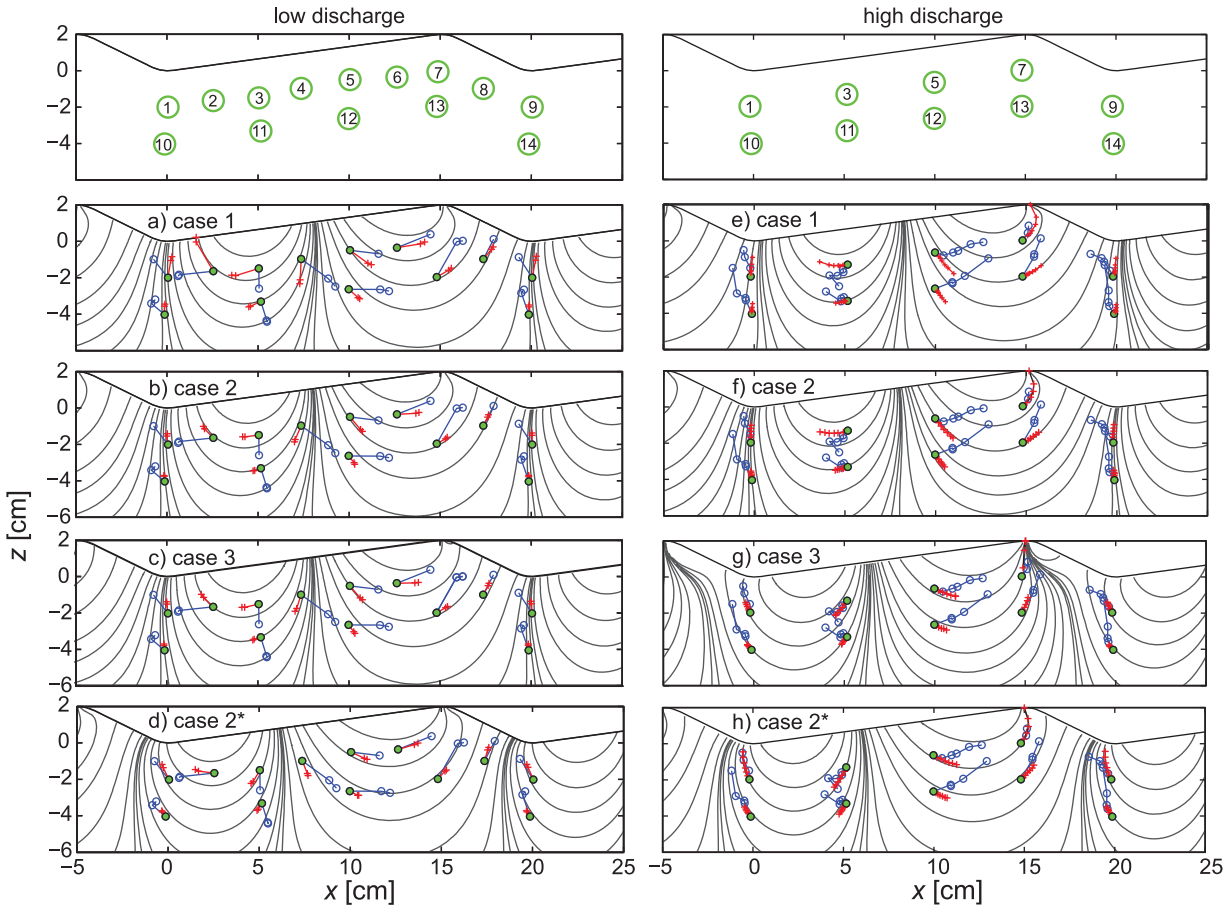

Figure 8. Comparison of dye tracks (blue lines and circles) and simulated particle tracks (red lines and crosses) for (a–d) low-discharge and (e–h) high-discharge conditions. The particle tracks are for Cases 1, 2, 3, and 2* (modified pressure profile). (top) Injection points are denoted by green-filled or outlined circles and are numbered; the shallower set of injections in the high-discharge case (injection points 1, 3, 5, 7, and 9) are the same as those in Figure 7. In the low-discharge experiments (Figures 8a–8d), each marker (dye and particle track) along the path away from the injection point corresponds to the location of the center of mass of the dye or the particle at t = 10 and 12 h. In the high-discharge experiments (Figures 8e–8h), each marker corresponds to the location of the center of mass of the dye or particle at t = 1, 2, 3, 4, and 6 h for the shallower set of injections. For the deeper set of injections, the marker locations correspond to t = 2, 3, 4, and 6 h. Note that at injection points 1, 7 and 9, under high-discharge conditions, the dye track could only be plotted up to the last time it was detected (i.e., before the dye was lost to the overlying water). In case of injection point 7, under low-discharge, all dye was lost already after 10 h, and only the injection position could be indicated.

general pore water flow patterns. The distribution of pore water velocity magnitude is largely similar for the simulations at low and high discharge, respectively (Figures 9a–9c and 9e–9g; Figures 9d and 9h refer to the modified Case 2* that is discussed in section 3.4). Only for Case 1 with mass flux boundary conditions at the inlet, simulated pore water velocities near the sediment-water interface are significantly higher (Figures 9a and 9e). This corresponds to more pronounced pressure peaks in Case 1 simulations (Figure 6).

[31] The locations of flow cell divides at the stoss faces ($x \sim 7$ cm for the sixth ripple) are similar for Cases 1, 2, and 3 at low discharge and Cases 1 and 2 at high-discharge conditions (Figures 9a–9c and 9e–9f). These locations coincide with the position of the simulated pressure peaks. Consequently, this position is shifted upstream in the simulation with a coarse mesh at high-discharge conditions (Figure 9g, Case 3) where the pressure rise and peak were also located further upstream and agreed more closely with measurements. The better agreement of pressure simulations and measurements in Case 3 at high discharge is also reflected in pore water flow patterns at the sixth ripple (Figure 8g). Dye tracks agree quite well with flow lines and particle tracks (red lines) obtained by simulations with coarse mesh especially at injection points 3, 5, and 12 in the region of the flow cell divide. In all other cases (Figures 8a–8c and 8e–8f), a comparison of dye tracks with flow lines clearly indicates that the flow cell divide in the experiments is farther upstream than in simulations. At injection points 3 and 11, the dye was displaced almost directly downward, indicating that the injection points are directly underneath the flow cell divide. Simulated particle tracks, on the other hand, are pointing downward at position 4, 25 mm farther downstream.

[32] Apart from the location of the flow cell divide, the main differences between the experimental results and the simulated

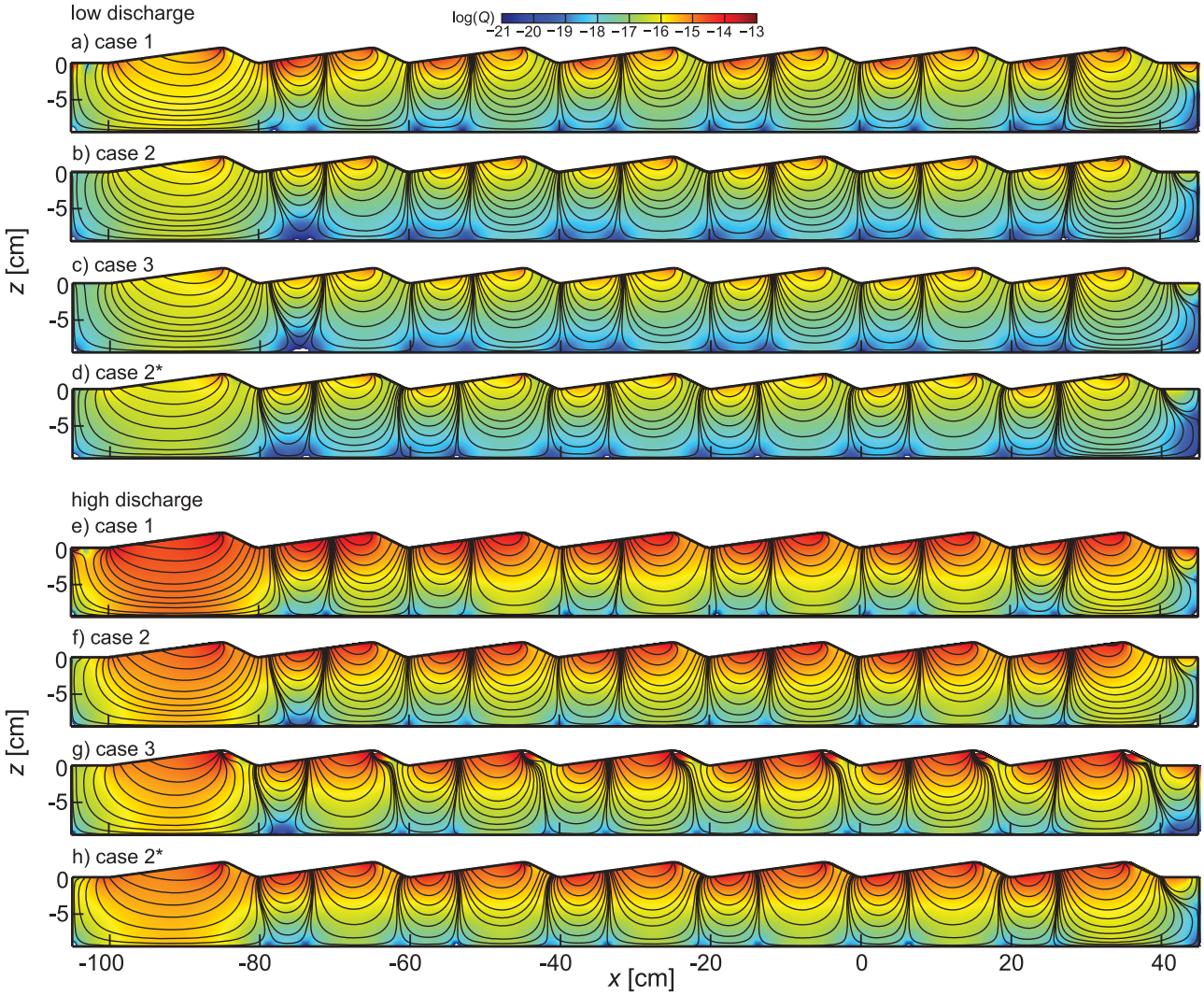

Figure 9. Simulated Darcy velocities (Q, m/s) for the entire sediment section of the flume at (a–d) low-discharge and (e–h) high-discharge conditions for the same cases as in Figure 5 (see Table 1 for boundary condition information). The scale represents the natural logarithm of Q.

pore water flow patterns concern the outflow area and overall pore water velocities. Both under low- and high-discharge conditions, the simulated pore water outflows are generally less focused toward the crest than dye tracks indicate (injection points 7–9 and 13–14). In some cases, convergence of the simulated pore water flow lines even indicate a second outflow center at the trough that clearly disagrees with experimental results. In case of the coarse mesh at high discharge (Case 3), the pronounced and probably overestimated pressure dip leads to a stronger convergence toward the crest (Figure 8g). A comparison of lengths of dye tracks and simulated particle tracks shows that predicted pore water velocities are generally smaller than those observed in the experiments. This discrepancy seems to be more pronounced deeper in the sediment than closer to the sediment-water interface. At some injection points, the simulated particles hardly moved whereas the dye was transported significantly (e.g., injection points 10, 11, and 14 in Figure 8b). The least discrepancy between pore water velocities occurs for Case 1 under low-discharge conditions. Here, the particle and dye had similar travel distances at several locations (e.g., points 1, 5, 6, 8, and 9 in Figure 8a).

3.4. Sensitivity to Pressure Along the Interface: A Modified Pressure and Flow Field

[33] The sensitivity of the simulated pore water flow field to the pressure along the interface was further assessed by visually correcting the pressure profiles simulated with fine mesh (Case 2) to fit the measurements better. This manual correction moved the location of the pressure peak at the stoss face upstream without changing its amplitude or the location of the pressure minimum. To obtain this, correction values were subtracted from the original x positions of the simulated pressures in the region around the pressure peak. Away from the x position where the largest correction value was subtracted (the region of the pressure peak), correction values decreased following a Gaussian distribution. The position and magnitude of the peak and the standard deviation of the Gaussian distribution of x correction values were adjusted manually until the best agreement between the modified pressure distribution and the measurements was obtained. Applying the same correction to the pressure distributions of all ripples resulted in a pressure distribution that covered the entire test section. The corrected pressure

Table 2. Average Fluxes and Residence Time for the Different Simulation Cases

Case	Discharge	Average Flux (cm d^{-1})	Residence Time (d)
1	low	0.95	10.2
2	low	0.51	18.8
3	low	0.51	18.8
2*	low	0.51	18.9
1	high	2.21	4.4
2	high	1.61	6.0
3	high	2.11	4.6
2*	high	1.58	6.1

profiles and the resulting pore water flow fields are denoted by an asterisk (2*) in the text and in the figures. The correction resulted in a close agreement of the shape of the pressure rise and the position of the pressure peak (Figure 5).

[34] Translation of the pressure peak upstream in the modified profiles leads to a similar translation of the pore water flow divide in the subsurface zone (Figures 9d and 9h). This in turn improves the agreement in the trajectories of the dye and particle tracks (compare Figure 8b with 8d and Figure 8f with 8h). No corrections were applied to the amplitude of the pressure profiles, and simulated particle travel distances remained much shorter than dye travel distances.

3.5. Model Fluxes and Residence Times

[35] The total influx ($m^2\ s^{-1}$) across the sediment-water interface, which is equal to total efflux, is calculated by integrating the magnitude of (normal) outward flux across the interface of the entire test section and then dividing the result by 2. The average influx ($m\ s^{-1}$) is calculated by dividing the total flux by the total length of the interface (1.5 m). The characteristic residence time is the area of the entire subsurface 2-D domain divided by the total influx.

[36] In the low-discharge conditions where Case 1 poorly represents the experimental conditions relative to the other cases (Figures 3 and 5), Case 1 resulted in higher flux and consequently lower residence time relative to Cases 2 and 3 (Table 2). The total flux in Case 1 is about 86% larger than the rest. However, fluxes and residence times are practically the same for Cases 2 and 3. Moreover, Case 2*, where pressure has been manually modified, has identical results as Case 2.

[37] Under high-discharge conditions, where errors in Case 1 relative to the experiments are still obvious but somewhat less prominent (Figures 4 and 5), the differences in fluxes and residence time are also smaller (Table 2). Case 1 still leads to higher total flux, and lower residence time, but this time by only as much as 37%. In fact, Cases 1 and 3 have similar fluxes. Manual modification of the pressure profile along the sediment-water interface to make it agree better with observations, i.e., Case 2*, leads to small changes (<2%) in total flux and residence time compared to the original Case 2.

4. Discussion and Conclusions

[38] The flume experiments were designed to simultaneously interrogate both surface and subsurface flow and transport processes with a full suite of parameters measured using minimally invasive instrumentation. The measurements form a unique data set that fully describes the system of coupled surface–subsurface flow and enables direct comparison with model outputs. All measurements were performed along the centerline of the flume, ruling out wall effects. The novel pore water displacement technique for visualizing the subsurface flow field represents a major step forward as compared to previous studies that were limited to measurements directly at the sidewall of the flume [e.g., *Savant et al.*, 1987; *Huettel and Gust*, 1992; *Precht and Huettel*, 2003]. In case of pore water flow, this may be particularly important, as the flume wall not only changes the pore water flow field due to differential porosity and permeability but also pressure and fluid flow due to the no-slip effect. The pressure measurement approach provided the pressure gradient along the surface of a sandy, unsolidified, permeable bed form and resulted in highly reproducible measurements that resolved the sharp dip at the crest, previously observed only in simulations [e.g., *Cardenas and Wilson*, 2007b].

[39] The limited length of the flume allowed for more rapid replicate experiments and facilitated modeling of the entire experimental setup and, hence, comparison to measurements. On the other hand the short channel caused the velocity profile at the inlet to impact the flow field throughout the test section. Consequently, surface flow and pressure simulations using a well-matched inlet velocity profile clearly show a better agreement to measurements. The ensuing discussion therefore only considers simulations with prescribed inlet velocity profile.

[40] The main characteristics of the experimental surface–subsurface system are properly resolved by the chosen multiphysics modeling framework. RANS simulations of turbulent flow match the measured mean velocity fields reasonably well and capture the eddy at the lee side of the ripple. The overall amplitude and the general pattern of the interfacial pressure gradient along the test ripple with a broad peak at the stoss side of the bed form and a sharp dip at the crest are well represented in simulations. The subsurface flow pattern with two counter-circulating pore water flow cells that divide at the stoss side occurs in both measurements and simulations and agrees with previous models and measurements [e.g., *Cardenas and Wilson*, 2007b; *Fehlman*, 1985; *Elliott and Brooks*, 1997b].

[41] Despite this good overall agreement, some deviations between simulations and measurements appear in distributions of surface and subsurface flow velocities as well as interfacial pressures. All observed differences, however, clearly relate to the overestimation of the eddy size in the CFD model. In agreement with the measurements the surface flow detachment and, hence, the point where the eddy starts to develop, is located at the crest throughout all simulations. Consequently, the overestimation of the eddy size shifts the reattachment point farther downstream in simulations as compared to measurements. This translates the simulated pressure maximum farther downstream and leads to a similar shift in the position of the subsurface flow cell divide and in an underestimation of the size of the counter-clockwise rotating pore water flow cell. This consistency in deviations reveals that an improper representation of the eddy size by the RANS simulation is the main but also singular substantial shortcoming of the applied multiphysics modeling approach. This is confirmed convincingly by a comparison of subsurface flow simulations obtained with a modified pressure distribution (Case 2* instead of Case 2).

A simple upstream shift of the peak in the simulated pressure gradients, as would result from a shorter eddy, largely improved the agreement of modeled and measured pore water flow patterns. The remaining differences in pore water flow velocities and circulation patterns may be attributed to a limited control over experimental conditions rather than to drawbacks of the model. The higher pore water flow velocities in the experiment probably indicate an underestimation of the true permeability of the sediment bed. Permeability was determined in packed cores. It is plausible that packing of the cores resulted in a higher compaction than in the flume. Test measurements performed with the same sand showed that permeabilities of uncompacted sediments were more than twice those of previously compacted sediments. Differences in pore water flow patterns could be explained by heterogeneities in sediment permeability and porosity in the experiments. These are not represented in the simulations that assume homogeneous and isotropic conditions. In order to minimize heterogeneity, sediment with a very narrow grain size distribution was chosen. However, it is still possible that variations in permeability and porosity were introduced in the process of bed form creation, where some trade off existed between a uniform compaction and precise shaping of the ripples.

[42] Changes in boundary conditions for the turbulent flow model also affect the resultant interfacial exchange flux and the characteristic residence time for exchange. However, even when the turbulent flow model shows inaccuracies, the resultant exchange fluxes are still within a factor of two compared to models where pressure along the interface was manually modified to represent actual conditions better. This is still a relatively small error in light of other sources of error under field conditions (e.g., sediment permeability). Therefore, if the boundary conditions for the turbulent flow model and the topography of the sediment-water interface are sufficiently close to actual conditions, reasonably good fluxes and residence times may be estimated with the multiphysics modeling framework. However, this also largely rests on accurate estimates of sediment hydraulic properties and associated critical assumptions such as homogeneity and isotropy.

[43] The direct comparison of experiments and simulations shows that any multiphysics modeling framework is only as good as its weakest component. In the case of modeling coupled surface–subsurface processes where bed form-covered sediments are exposed to unidirectional flow, it is critical that any eddies in the surface water are resolved well. Rather than comparing various CFD approaches (there are more than a dozen ways to numerically model turbulent flow), this study focuses on the RANS k-ω approach since it balances computational efficiency with good performance for detached (eddy) flows [*Wilcox*, 1991, 1998]. More sophisticated methods like large-eddy simulations (LES) or direct numerical simulations were considered less appropriate, since the hydraulic diffusivity of the flume sediment limits the response of subsurface flow paths to very high-frequency pressure oscillations. Flow and pressure variations at lower frequencies such as in wave-driven flow in coastal environments, however, may affect subsurface flow and transport, as shown in *Cardenas and Jiang* [2011] and may call for more complex simulation methods.

[44] The RANS k-ω approach adopted in this study performs well in comparison to previous studies. The modeled stream-wise mean velocities are qualitatively better than similar comparisons of RANS-based CFD simulations with flume experiments [cf. *Yoon and Patel*, 1996, Figure 6; *Cokljat and Kralj*, 1997, Figure 2] and even better than or just as good as recent CFD simulations using more sophisticated and computationally intensive methods (LES) [cf. *Yue et al.*, 2006, Figure 3; *Stoesser et al.*, 2008, Figure 4; *van Balen et al.*, 2010, Figure 17]. However, the earlier studies mentioned above modeled experimental conditions at higher Reynolds numbers, and each study used different bed form geometries. A recent LES study of flow over dunes also yielded superior agreement between modeled and measured mean velocity profiles [*Grigoriadis et al.*, 2009, Figure 5] and also captured three velocity profiles within the eddy better than any study the authors are familiar with, including this study. Most CFD simulations of flow over ripples and dunes show the largest discrepancy in the eddy zone. This is a known weakness of all RANS-based approaches including the one adopted for this study. RANS models assume isotropic turbulence, which is prone to violation in the near-wall region of recirculation zones; however, this is also apparently a difficult zone to model for some LES approaches [*Stoesser et al.*, 2008].

[45] While only one formulation for modeling turbulence was used, various treatments for the wall boundary representing the sediment surface were considered to investigate the sensitivity of the CFD model. Tested wall boundaries include smooth walls, rough walls, and fine or coarse numerical grids near the wall. On the whole, the observed effects on surface flow, interfacial pressure distribution, and subsurface flow are relatively small. Simulations with different wall roughness produced results that were virtually indistinguishable. On one hand, this shows the robustness of the CFD model used in this study. On the other hand, none of the tested wall boundaries was able to substantially improve the agreement to experimental results. All cases overestimated the eddy size, simulated the pressure peak's location slightly downstream of the observed peak, and underestimated the magnitude of the pressure high at the test ripple. The sole exception is Case 3 at high discharge. In this case, the coarser grid leads to a better agreement to measured velocities and most accurately captures eddy recirculation and reattachment as well as the location of the pressure peak. On the other hand, this case underestimates the magnitude of the pressure peak while largely overestimating the magnitude of a pressure dip near the crest where the eddy detaches. It is plausible that a coarser resolution of the near-wall recirculation region effectively increases turbulent diffusion and limits the size of the eddy. Essentially, adopting the coarse grid at high discharge most likely produces the "right" answer for the "wrong" reasons. The larger pressure dip may be indicative of a numerical artifact that increases in magnitude with coarser resolution of the eddy detachment. These results emphasize the grid sensitivity of turbulence models for larger Reynolds numbers and the importance of acquiring high-resolution experimental data for comparison with CFD models whenever extreme accuracy is needed in simulations. However, the consistency in deviations between simulations and measurements that was observed in this study suggests that future comparisons can be restricted to one parameter only, i.e., surface flow, pressure distribution, or subsurface flow.

[46] Although a perfect representation of the eddy and hence the surface and subsurface flow is not achievable with this modeling approach, the model performance is acceptable for characterizing bulk properties of surface–subsurface flow in current-exposed bed forms. The approach is therefore useful in studies of, e.g., particle filtration rates or net solute fluxes across the sediment-water interface. In more complex problems that depend on small-scale pore water transport patterns, improved model performance may be necessary. In a modeling study of permeable bed forms under oscillating flow, *Cardenas et al.* [2008b] demonstrated that in order to predict sediment denitrification rates, a detailed knowledge of the boundary conditions, subsurface flow, and transport properties is required. In such cases, a correct model representation of the physical processes is essential to predict the predominant biogeochemical processes and to correctly estimate the element cycling at a larger scale.

[47] Being aware of these limitations and the potential need for validation, multiphysics modeling represents a promising and viable approach for analyzing coupled surface–subsurface flow and transport processes. It is almost impossible to measure millimeter-scale pressure variations and pore water flow patterns in natural settings. However, very detailed bathymetric mapping in natural environments is becoming commonplace [e.g., *Jerolmack and Mohrig*, 2005; *Nittrouer et al.*, 2008]. These data sets can easily be used in multiphysics CFD models. With the advent of applications of 3-D CFD models at the channel scale [e.g., *van Balen et al.*, 2010; *Kang et al.*, 2011], implementation of a multiphysics model of 3-D surface–subsurface flow and transport processes is now possible.

[48] Here, a unique experimental data set is used to investigate the applicability of a state of the art multiphysics CFD modeling framework for investigations of coupled surface–subsurface flows. The simulations reproduced flow and transport processes fairly well throughout the entire flume. Most insights into physical processes from the flume experiments could have been similarly discovered through multiphysics modeling with differences that would be insignificant for many process studies. Therefore, it is concluded that multiphysics CFD models represent coupled surface–subsurface flow relatively well and should continue to be used for analysis of increasingly complex and multidimensional problems. In order to validate and further improve future modeling approaches experimental data will remain indispensable.

[49] **Acknowledgments.** F.J. was supported by EU projects ECODIS (FP6, contract 518043) and HYPOX (FP7, contract 226213). M.B.C. was supported by a National Science Foundation CAREER grant (EAR-0955750). A.H.S. was partly supported by a National Science Foundation Graduate Research Fellowship. We thank Martina Alisch and Angela Schramm (MPI) for help with the preparation of the fluorescence sensors and the conduction of the experiments. Volker Meyer, Paul Färber, and Georg Herz are acknowledged for their development of the controlling unit and the mechanical parts of the dye tracing instrument. The authors would like to thank Tobias Graf for helpful comments on previous versions of the manuscript. We thank Ted Endreny and two anonymous reviewers for constructive reviews.

References

Bardini, L., F. Boano, M. B. Cardenas, R. Revelli, and L. Ridolfi (2012), Nutrient cycling in bedform induced hyporheic zones, *Geochim. Cosmochim. Acta*, *84*, 47–61, doi:10.1016/j.gca.2012.01.025.

Boano, F., R. Revelli, and L. Ridolfi (2007), Bedform-induced hyporheic exchange with unsteady flows, *Adv. Water Resour.*, *30*, 148–156, doi:10.1016/j.advwatres.2006.03.004.

Boano, F., R. Revelli, and L. Ridolfi (2010), Effect of streamflow stochasticity on bedform-driven hyporheic exchange, *Adv. Water Resour.*, *33*, 1367–1374, doi:10.1016/j.advwatres.2010.03.005.

Cardenas, M. B., and M. N. Gooseff (2008), Comparison of hyporheic exchange under covered and uncovered channels based on linked surface and groundwater flow simulations, *Water Resour. Res.*, *44*, W03418, doi:10.1029/2007WR006506.

Cardenas, M. B., and H. S. Jiang (2011), Wave-driven porewater and solute circulation through rippled elastic sediment under highly transient forcing, *Limnol. Oceanogr. Fluids Environ.*, *1*, 23–37, doi:10.1215/21573698-1151658.

Cardenas, M. B., and J. L. Wilson (2007a), Thermal regime of dune-covered sediments under gaining and losing water bodies, *J. Geophys. Res.*, *112*, G04013, doi:10.1029/2007JG000485.

Cardenas, M. B., and J. L. Wilson (2007b), Dunes, turbulent eddies, and interfacial exchange with permeable sediments, *Water Resour. Res.*, *43*, W08412, doi:10.1029/2006WR005787.

Cardenas, M. B., J. L. Wilson, and R. Haggerty (2008a), Residence time of bedform-driven hyporheic exchange, *Adv. Water Resour.*, *31*, 1382–1386, doi:10.1016/j.advwatres.2008.07.006.

Cardenas, M. B., P. L. M. Cook, H. Jiang, and P. A. Traykovski (2008b), Constraining denitrification in permeable wave-influenced marine sediment using linked hydrodynamic and biogeochemical modeling, *Earth Planet. Sci. Lett.*, *275*, 127–137, doi:10.1016/j.epsl.2008.08.016.

Chen, C., A. I. Packman, and J.-F. Gaillard (2008), Pore-scale analysis of permeability reduction resulting from colloid deposition, *Geophys. Res. Lett.*, *35*, L07404, doi:10.1029/2007GL033077.

Chen, C., A. I. Packman, and J. Gaillard (2009), Using X-ray microtomography and pore-scale modeling to quantify sediment mixing and fluid flow in a developing streambed, *Geophys. Res. Lett.*, *36*, L08403, doi:10.1029/2009GL037157.

Cokljat, D., and C. Kralj (1997), On choice of turbulence model for prediction of flows over river bed forms, *J. Hydraul. Res.*, *35*, 355–361, doi:10.1080/00221689709498417.

Crispell, J. K., and T. A. Endreny (2009), Hyporheic exchange flow around constructed in-channel structures and implications for restoration design, *Hydrol. Processes*, *23*, 1158–1168, doi:10.1002/hyp.7230.

Elliott, A. H., and N. H. Brooks (1997a), Transfer of nonsorbing solutes to a streambed with bed forms: Theory, *Water Resour. Res.*, *33*, 123–136, doi:10.1029/96WR02784.

Elliott, A. H., and N. H. Brooks (1997b), Transfer of nonsorbing solutes to a streambed with bed forms: Laboratory experiments, *Water Resour. Res.*, *33*, 137–151, doi:10.1029/96WR02783.

Endreny, T., L. Lautz, and D. I. Siegel (2011), Hyporheic flow path response to hydraulic jumps at river steps: Flume and hydrodynamic models, *Water Resour. Res.*, *47*, W02517, doi:10.1029/2009WR008631.

Fehlman, H. M. (1985), Resistance components and velocity distributions of open channel flows over bedforms, Ph.D. thesis, Colo. State Univ., Fort Collins.

Franke, U., L. Polerecky, E. Precht, and M. Huettel (2006), Wave tank study of particulate organic matter degradation in permeable sediments, *Limnol. Oceanogr.*, *51*, 1084–1096, doi:10.4319/lo.2006.51.2.1084.

Grigoriadis, D. G. E., E. Balaras, and A. A. Dimas (2009), Large-eddy simulations of unidirectional water flow over dunes, *J. Geophys. Res.*, *114*, F02022, doi:10.1029/2008JF001014.

Huettel, M., and G. Gust (1992), Impact of bioroughness on interfacial solute exchange in permeable sediments, *Mar. Ecol. Prog. Ser.*, *89*, 253–267, doi:10.3354/meps089253.

Huettel, M., and I. T. Webster (2001), Porewater flow in permeable sediments, in *The Benthic Boundary Layer: Transport Processes and Biogeochemistry*, edited by B. P. Boudreau and B. B. Jørgensen, pp. 144–179, Oxford Univ. Press, New York.

Huettel, M., W. Ziebis, S. Forster, and G. W. Luther (1998), Advective transport affecting metal and nutrient distributions and interfacial fluxes in permeable sediments, *Geochim. Cosmochim. Acta*, *62*, 613–631, doi:10.1016/S0016-7037(97)00371-2.

Jerolmack, D. J. and D. Mohrig (2005), A unified model for subaqueous bed form dynamics, *Water Resour. Res.*, *41*, W12421, doi:10.1029/2005WR004329.

Jin, G., H. Tang, L. Li, and D. A. Barry (2011), Hyporheic flow under periodic bed forms influenced by low-density gradients, *Geophys. Res. Lett.*, *38*, L22401, doi:10.1029/2011GL049694.

Kang, S., A. Lightbody, C. Hill, and F. Sotiropoulos (2011), High-resolution numerical simulation of turbulence in natural waterways, *Adv. Water Resour.*, *34*, 98–113, doi:10.1016/j.advwatres.2010.09.018.

Karwan, D. L. and J. E. Saiers (2012), Hyporheic exchange and streambed filtration of suspended particles, *Water Resour. Res.*, *48*, W01519, doi:10.1029/2011WR011173.

Marion, A., A. I. Packman, M. Zaramella, and A. Bottacin-Busolin (2008), Hyporheic flows in stratified beds, *Water Resour. Res.*, *44*, W09433, doi:10.1029/2007WR006079.

Mojid, M. A., and H. Vereecken (2005), Modelling velocity and retardation factor of a nonlinearly sorbing solute plume, *Aust. J. Soil Res.*, *43*, 735–743, doi:10.1071/SR04111.

Mutz, M., E. Kalbus, and S. Meinecke (2007), Effect of instream wood on vertical water flux in low-energy sand bed flume experiments, *Water Resour. Res.*, *43*, W10424, doi:10.1029/2006WR005676.

Nittrouer, J. A., M. A. Allison, and R. Campanella (2008), Bedform transport rates for the lowermost Mississippi River, *J. Geophys. Res.*, *113*, F03004, doi:10.1029/2007JF000795.

Packman, A. I., and J. S. MacKay (2003), Interplay of stream-subsurface exchange, clay particle deposition, and streambed evolution, *Water Resour. Res.*, *39*(4), 1097, doi:10.1029/2002WR001432.

Packman, A. I., N. H. Brooks, and J. J. Morgan (2000), Kaolinite exchange between a stream and streambed: Laboratory experiments and validation of a colloid transport model, *Water Resour. Res.*, *36*, 2363–2372, doi:10.1029/2000WR900058.

Precht, E., and M. Huettel (2003), Advective pore-water exchange driven by surface gravity waves and its ecological implications. *Limnol. Oceanogr.*, *48*, 1674–1684.

Precht, E., and M. Huettel (2004), Rapid wave-driven advective pore water exchange in a permeable coastal sediment, *J. Sea Res.*, *51*, 93–107, doi:10.1016/j.seares.2003.07.003.

Precht, E., U. Franke, L. Polerecky, and M. Huettel (2004), Oxygen dynamics in permeable sediments with wave-driven pore water exchange, *Limnol. Oceanogr.*, *49*, 693–705, doi:10.4319/lo.2004.49.3.0693.

Reidenbach, M. A., M. Limm, M. Hondzo, and M. T. Stacey (2010), Effects of bed roughness on boundary layer mixing and mass flux across the sediment-water interface, *Water Resour. Res.*, *46*, W07530, doi:10.1029/2009WR008248.

Ren, J. H., and A. I. Packman (2005), Coupled stream-subsurface exchange of colloidal hematite and dissolved zinc, copper, and phosphate, *Environ. Sci. Technol.*, *39*, 6387–6394, doi:10.1021/es050168q.

Salehin, M., A. I. Packman, and M. Paradis (2004), Hyporheic exchange with heterogeneous streambeds: Laboratory experiments and modeling, *Water Resour. Res.*, *40*, W11504, doi:10.1029/2003WR002567.

Savant, S. A., D. D. Reible, and L. J. Thibodeaux (1987), Convective transport within stable river sediments, *Water Resour. Res.*, *23*, 1763–1768, doi:10.1029/WR023i009p01763.

Sawyer, A. H. and M. B. Cardenas (2009), Hyporheic flow and residence time distributions in heterogeneous cross-bedded sediment, *Water Resour. Res.*, *45*, W08406, doi:10.1029/2008WR007632.

Sawyer, A. H., M. B. Cardenas, and J. Buttles (2011), Hyporheic exchange due to channel-spanning logs, *Water Resour. Res.*, *47*, W08502, doi:10.1029/2011WR010484.

Sawyer, A. H., M. Bayani Cardenas, and J. Buttles (2012), Hyporheic temperature dynamics and heat exchange near channel-spanning logs, *Water Resour. Res.*, *48*, W01529, doi:10.1029/2011WR011200.

Shen, H. W., H. M. Fehlman, and C. Mendoza (1990), Bed form resistance in open channel flows, *J. Hydraul. Eng.*, *116*, 799–815, doi:10.1061/(ASCE)0733-9429(1990)116:6(799).

Stoesser, T., C. Braun, M. Garcia-Villalba, and W. Rodi (2008), Turbulence structures in flow over two-dimensional dunes, *J. Hydraul. Eng.*, *134*, 42–55, doi:10.1061/(ASCE)0733-9429(2008)134:1(42).

Stonedahl, S. H., J. W. Harvey, A. Wörman, M. Salehin, and A. I. Packman (2010), A multiscale model for integrating hyporheic exchange from ripples to meanders, *Water Resour. Res.*, *46*, W12539, doi:10.1029/2009WR008865.

Thibodeaux, L. J., and J. D. Boyle (1987), Bedform-generated convective transport in bottom sediment, *Nature*, *325*, 341–343, doi:10.1038/325341a0.

Tonina, D., and J. M. Buffington (2007), Hyporheic exchange in gravel bed rivers with pool-riffle morphology: Laboratory experiments and three-dimensional modeling, *Water Resour. Res.*, *43*, W01421, doi:10.1029/2005WR004328.

Tonina, D., and J. M. Buffington (2009), A three-dimensional model for analyzing the effects of salmon redds on hyporheic exchange and egg pocket habitat, *Can. J. Fish. Aquat. Sci.*, *66*, 2157–2173, doi:10.1139/F09-146.

Toth, J. (1963), A theoretical analysis of groundwater flow in small drainage basins, *J. Geophys. Res.*, *68*, 4795–4812.

van Balen, W., W. S. J. Uijttewaal, and K. Blanckaert (2010), Large-eddy simulation of a curved open-channel flow over topography, *Phys. Fluids*, *22*(7), 075108, doi:10.1063/1.3459152.

Vaux, W. G. (1968), Intragravel flow and interchange of water in a streambed, *Fish. Bull.*, *66*, 479–489.

Vereecken, H., U. Jaekel, O. Esser, and O. Nitzsche (1999), Solute transport analysis of bromide, uranin and LiCl using breakthrough curves from aquifer sediment, *J. Contam. Hydrol.*, *39*, 7–34, doi:10.1016/S0169-7722(99)00033-9.

Vittal, N., K. G. R. Raju, and R. J. Garde (1977), Resistance of 2 dimensional triangular roughness, *J. Hydraul. Res.*, *15*, 19–36, doi:10.1080/00221687709499747.

Wilcox, D. C. (1991), A half century historical review of the k-ω model, *AIAA Pap. 91-0615*, NASA, Greenbelt, Md.

Wilcox, D. C. (1998), *Turbulence Modeling for CFD*, 540 pp., DCW Industries, Inc., La Canada, Calif.

Worman, A., A. I. Packman, L. Marklund, J. W. Harvey, and S. H. Stone (2006), Exact three-dimensional spectral solution to surface-groundwater interactions with arbitrary surface topography, *Geophys. Res. Lett.*, *33*, L07402, doi:10.1029/2006GL025747.

Yoon, J. Y., and V. C. Patel (1996), Numerical model of turbulent flow over sand dune, *J. Hydraul. Eng.*, *122*, 10–18, doi:10.1061/(ASCE)0733-9429(1996)122:1(10).

Yue, W. S., C. L. Lin, and V. C. Patel (2006), Large-eddy simulation of turbulent flow over a fixed two-dimensional dune, *J. Hydraul. Eng.*, *132*, 643–651, doi:10.1061/(ASCE)0733-9429(2006)132:7(643).

Zlotnik, V. A., M. B. Cardenas, and D. Toundykov (2011), Effects of multiscale anisotropy on basin and hyporheic groundwater flow, *Ground Water*, *49*, 576–583, doi:10.1111/j.1745-6584.2010.00775.x.